



HAL
open science

On the precipitation and transformation kinetics of precipitationhardening steel X5CrNiCuNb16-4 in a wide range of heating and cooling rates

Benjamin Milkereit, Christian Rowolt, Dipanwita Chatterjee, Randi Holmestad, Ruben Bjørge, Matteo Villa, Frank Niessen, Andreas Stark, Frédéric de Geuser, Olaf Kessler

► To cite this version:

Benjamin Milkereit, Christian Rowolt, Dipanwita Chatterjee, Randi Holmestad, Ruben Bjørge, et al.. On the precipitation and transformation kinetics of precipitationhardening steel X5CrNiCuNb16-4 in a wide range of heating and cooling rates. *Materialia*, 2024, 38, pp.102254. 10.1016/j.mtla.2024.102254 . hal-04781159

HAL Id: hal-04781159

<https://hal.science/hal-04781159v1>

Submitted on 13 Nov 2024

HAL is a multi-disciplinary open access archive for the deposit and dissemination of scientific research documents, whether they are published or not. The documents may come from teaching and research institutions in France or abroad, or from public or private research centers.

L'archive ouverte pluridisciplinaire **HAL**, est destinée au dépôt et à la diffusion de documents scientifiques de niveau recherche, publiés ou non, émanant des établissements d'enseignement et de recherche français ou étrangers, des laboratoires publics ou privés.

On the precipitation and transformation kinetics of precipitation-hardening steel X5CrNiCuNb16-4 in a wide range of heating and cooling rates

Benjamin Milkereit^{1,2}, Christian Rowolt^{1,2}, Dipanwita Chatterjee³, Randi Holmestad³, Ruben Bjørge⁴, Matteo Villa⁵, Frank Niessen⁵, Andreas Stark⁶, Frédéric De Geuser⁷, Olaf Kessler^{1,2}

¹ °CALOR, Department LL&M, University of Rostock, Germany

² Chair of Materials Science, University of Rostock, Germany

³ Department of Physics, Norwegian University of Science and Technology NTNU, Høgskoleringen 5, 7491 Trondheim, Norway

⁴ Department of Materials and Nanotechnology, SINTEF Industry, P.O. Box 4760 Torgarden, NO-7465 Trondheim, Norway

⁵ Department of Mechanical Engineering, Materials and Surface Engineering, Technical University of Denmark DTU, Copenhagen, Denmark

⁶ Institute of Materials Physics, Helmholtz-Zentrum Hereon, Geesthacht, Germany

⁷ Univ. Grenoble Alpes, Grenoble INP, SIMaP, 38000 Grenoble, France

Abstract

In this work, the transformation and dissolution/precipitation behaviour of the soft martensitic, precipitation-hardening steel X5CrNiCuNb16-4 (often referred to as 17-4 PH or AISI 630) has been investigated by various analytical in situ techniques. First, austenite formation during the heating stage of a solution treatment (or austenitization) is examined. Subsequently, a major part of this work evaluates precipitation during cooling from the solution treatment (i.e., the quench-induced precipitation of Cu-rich particles). The following analytical in situ techniques were utilised: synchrotron high-energy X-ray diffraction, synchrotron small-angle X-ray scattering, differential scanning calorimetry, and dilatometry. These were complemented by ex situ high-angle annular dark-field scanning transmission electron microscopy coupled with energy-dispersive X-ray spectroscopy on as-quenched samples after various cooling rates. The continuous heating transformation and continuous cooling transformation diagrams have been updated. Contrary to previous reports, X5CrNiCuNb16-4 is rather quench sensitive and the final properties after ageing degrade if cooling is done slower than a certain critical cooling rate. Quench-induced Cu-rich precipitation happens in two reactions: a larger, nearly pure Cu face-centred cubic phase forms at higher temperatures, while at medium temperatures, spherical Cu-rich nanoparticles form, which are found to be body-centred cubic at room temperature. The dimensions of the quench-induced particles range from several μm after cooling at 0.0001 K/s down to just a few nm after cooling at 1 K/s. The maximum age hardening

potential of X5CrNiCuNb16-4 can be exploited if a fully supersaturated solid solution is reached at cooling rates above the critical cooling rate of about 10 K/s.

Keywords:

X5CrNiCuNb16-4, 17-4PH; austenitization; quench-induced-precipitation

1 Introduction

Precipitation-hardening steels are iron-chromium-nickel alloys containing precipitation-hardening elements, such as aluminium, titanium, niobium, and copper (e.g., [1–3]). The strength of precipitation-hardening steels is adjusted by an age-hardening process. This process aims for a structure with nano-scaled precipitates that hinder dislocation gliding and increase the strength. The heat treatment comprises three major steps: solution treatment, quenching, and ageing. The solution treatment (which for steels typically takes place in the austenite region) aims to achieve a homogenous solid solution. During quenching, the alloying elements are ‘frozen in’, resulting in a supersaturated solid solution. In this state, the system is far from equilibrium and is thus unstable. From this state, during the final ageing treatment, a large number density of nano-scale precipitates form. In this work, precipitation-hardening steels that use Cu as a precipitation-hardening element are considered. The precipitation sequence during ageing remains a topic of recent research [2,4,5], although it can be simplified as [5–7]:

supersaturated martensitic phase → Cu-Fe-rich clusters → Cu-Fe-rich precursor precipitates, orthorhombic 9R structures → Cu-rich twinned face-centred cubic (fcc) precursors → fcc Cu

A core/shell structure with Ni surrounding fine Cu precipitates is also reported to occur within the sequence of Cu precipitation [8]. Furthermore, it has been recently shown that precipitation during cooling also occurs in a sequence of at least two reactions [9–12]. However, a comprehensive understanding of this sequence of quench-induced precipitation is still lacking.

To choose appropriate heat treatment parameters for specific steels during production, continuous heating transformation (CHT) and continuous cooling transformation (CCT) diagrams are typically used. However, because of disregarded effects, these diagrams are currently incomplete. This work aims to bridge these knowledge gaps by applying a broad range of analytical in situ techniques, improving the CHT and CCT diagrams. Using a variety of highly sensitive analytical techniques, rather than relying solely on dilatometry, is critical to accurately update the existing diagrams for precipitation-hardening steels.

2 Experimental methods

2.1 Investigated material

The martensitic, precipitation-hardening steel X5CrNiCuNb16-4 (often referred to as 17-4 PH or AISI 630) was analysed in two different batches. Samples were either taken out of a conventional hot rolled bar (dimensions of \varnothing 15 × 3000 mm) in an annealed (1038 °C, 1 h) and quenched condition or from laser beam melted (LBM) cylinders (dimensions of \varnothing 7 × 65 mm) in the as-built condition. The concentrations of alloying elements in both materials, as analysed by optical emission spectroscopy, are shown in Table 1. Both batches agreed with the standard DIN EN 10088-3.

Table 1: Alloying element concentration of the investigated X5CrNiCuNb16-4 batches (mass fraction in %)

| Sample | C | Si | Mn | Cr | Mo | Ni | Cu | Nb | Fe |
|--------------------------------------|----------|-----------|-----------|---------------|-----------|-------------|-------------|----------------|-----------|
| <i>Conventionally hot rolled bar</i> | 0.017 | 0.47 | 0.59 | 15.41 | 0.153 | 4.59 | 3.02 | 0.290 | bal. |
| <i>Laser beam melted</i> | 0.013 | 0.34 | 0.22 | 16.65 | 0.014 | 4.32 | 4.15 | 0.296 | bal. |
| <i>DIN EN 10088-3</i> | <0.07 | <0.7 | <1.5 | 15.0- 17.0 | <0.6 | 3.0- 5.0 | 3.0- 5.0 | 5 x C- 0.45 | bal. |

2.2 Differential scanning calorimetry and dilatometry

The transformation of steel X5CrNiCuNb16-4 during heating to the austenitization temperature and subsequent cooling to room temperature was investigated in the 30–1100 °C temperature range by both dilatometry and calorimetry. A Baehr DIL 805 A/D quenching dilatometer was used. Heating and cooling rates in the range of 0.1–100 K/s were investigated. Dilatometer samples with a diameter of 4 mm and a length of 10 mm were made from the cylindrical blanks. At least three individual samples were used for each scan rate. The execution and evaluation of the tests were based on the methods presented in [13,14].

The Setaram Labsys Evo and Setaram MultiHTC differential scanning calorimetry (DSC) instruments, equipped with highly sensitive Calvet DSC sensors [15], were used for DSC experiments. These instruments allow for scanning rates in the 0.003–0.3 K/s range. The dimensions of the sample and reference materials for the Setaram Labsys Evo were \varnothing 4.9 × 11.6 mm. The specimens were placed in ceramic crucibles, which themselves were inserted into platinum crucibles. The dimensions of the sample and reference materials for the Setaram MultiHTC were \varnothing 5.9 × 16 mm. The tests took place in argon atmospheres. At least four individual samples were compared to two baseline measurements for each scan rate investigated by DSC. The technical ceramic Rescor960 (Al₂O₃) was used as a reference

material. A detailed description of the execution and evaluation of the calorimetric experiments can be found in [10].

2.3 Hardness testing

Vickers hardness tests (ISO 6507-1) were carried out to assess the effect of different cooling rates on the mechanical properties using a Shimadzu HMV-2 microhardness tester. The samples were austenitized and cooled in a DSC or a dilatometer. Hardness testing was done in the as-quenched and artificially aged (480 °C, 60 min) conditions. Additional X5CrNiCuNb16-4 samples were heat treated in a controlled furnace to achieve very low cooling rates of 10^{-3} and 10^{-4} K/s. The samples were sealed in quartz tubes under an argon atmosphere to prevent oxidation.

2.4 High-energy X-ray diffraction

The in situ transmission high-energy X-ray diffraction (HE-XRD) investigation was performed at the BESSY-II synchrotron facility at the EDDI beamline [16]. The thermal cycle consisted of continuous heating at a constant rate of 0.1 K/s from 30 to 1050 °C. This operation was performed in an Anton Paar DHS 1100 Domed Hot Stage under a continuous flow of argon at a constant pressure of 1.4 bar. The samples were discs with a diameter of 15 mm and a thickness of 0.25 mm that were placed on the heating element (alumina plate), which they were fixed to via mild clamping. The temperature was measured with a Pt-Pt10Rh thermocouple fixed to the stage. HE-XRD was performed by applying energy-dispersive XRD [17], where the diffraction angle, 2θ , was fixed and the probed diffraction lines were generated simultaneously at different photon energies. For the present investigation, the acquisition time was set at 60 s per spectrogram and the experiments were conducted with a primary slit configuration of 0.5 × 0.5 mm, applying the diffraction geometry $\theta - 2\theta = 7^\circ - 14^\circ$. The equatorial slit aperture at the secondary side was set to 0.03 mm.

The transformation from martensite to austenite was followed by the evolution of the diffracted intensity for the reflections located in the energy range of 20–70 keV. For $2\theta = 14^\circ$, the following reflections fall within the range of interest: {111}, {200}, {220}, {311}, and {222} for austenite; {110}, {200}, {211}, {220}, and {321} for martensite. The quantitative phase analysis was based on the {200}, {220}, {311}, and {222} reflections of austenite and the {200}, {211}, {220}, and {321} reflections of martensite. The {111} austenite and the {110} martensite reflections were not considered because of their overlap. The diffracted intensity was evaluated by fitting the peak profiles with Pseudo-Voigt functions. The martensite crystal was approximated to cubic, which is justified given the low number of interstitial atoms in the steel. The volume fractions of austenite and martensite were determined with the direct comparison method [18], the details of which have been reported elsewhere [19].

Moreover, HE-XRD experiments on additively manufactured steel have been performed alongside small-angle X-ray scattering (SAXS) experiments, considering cooling at a rate of 0.03 K/s after annealing at 1100 °C for 30 min. Details on the evaluation have been published in [20].

2.5 Small-angle X-ray scattering

The general experimental setup for the SAXS experiments is published in detail in [20]. The cylindrical samples (\varnothing 4 × 10 mm) were austenitized and cooled at constant rates in a modified dilatometer (Baehr 805 A/D), which was mounted in the DESY synchrotron facility in Hamburg, Germany (Deutsches Elektronen-Synchrotron). The high energy materials science (HEMS) beamline P07 at PETRA III, which provides tuneable photon energies in the 30 to 200 keV range [21], was used. The high beam energy of 95.68 keV, corresponding to a wavelength of 0.012958 nm, allows the beam to penetrate a bulk steel sample with a 4 mm diameter, while the high intensity of a synchrotron source enables a sufficiently high time resolution for fast in situ cooling experiments. A tungsten beam stop with a diameter of 1 mm was used and the cross-section of the incident beam was set to 0.175 × 0.2 mm. SAXS patterns were recorded continually during the cooling experiments with an exposure time of 1 s for each measurement. A digital X-ray flat panel detector PE-XRD 1621 produced by Perkin Elmer Inc. was utilised. The detector centre position was determined using a silver behenate reference sample. From that, the distance between the sample and detector was evaluated to be 10,416 mm. The beam passed this distance through the air. For data correction, the transmission was analysed for each experiment by a separate diode scan correcting for air diffraction. In addition, a glassy carbon sample was measured as a standard for data correction.

SAXS patterns were background subtracted, azimuthally integrated, and normalised by the sample thickness and transmission, as well as by the solid angle. The obtained one-dimensional (1-D) intensity versus scattering vector, q , was further converted to absolute units through the use of glassy carbon as a secondary calibration sample [22]. Given the experimental setup, the achieved scattering vector range spanned from 0.005 to 0.6 Å⁻¹, giving access to precipitate sizes ranging from less than 1 nm up to ~100 nm. The wide range of heating and cooling rates used in this work may lead to a wide range of precipitate sizes, while the microstructure of the samples contains electron density heterogeneities (e.g., dislocations, segregations, and broader carbides), which form a material 'baseline' that may hinder detection of the larger precipitates.

The SAXS patterns were interpreted using a custom-implemented version of the McSAS software [23]. The underlying assumption is that all objects giving rise to SAXS signal are spherical. The McSAS algorithm uses a Monte Carlo procedure, wherein an assembly of precipitates has evolving sizes, which improves the fit of the resulting SAXS signal to the experimental data. Fixing the precipitate shape to spheres is a relatively good approximation

as SAXS is mostly used here to capture the formation of the very fine Cu precipitates. The broader heterogeneities, which are not necessarily spherical, are still fitted by the algorithm but with an altered size distribution. All the in situ SAXS patterns are fitted by the Monte Carlo procedure, with the resulting size distribution of each pattern being used as a starting point for the following pattern. The resulting volume-weighted size distributions may be stacked as a size-temperature-fraction map and are represented by isolines. The SAXS integrated intensity of the precipitates can be converted to volume fractions through the electron density contrast, which depends on the Cu content in the particles.

2.6 Scanning transmission electron microscopy

For the ex situ scanning transmission electron microscopy (STEM) analysis, ~100 μm thick discs were cut from 4 mm diameter cylinders, which were previously heat treated in a quenching dilatometer. Discs with a diameter of 3 mm were punched from the 4 mm discs and then dimpled at the centre with 3 μm diamond paste using a dimpler from Agar Scientific (model 2000) to a thickness of 20–30 μm . A GATAN PIPS II 695 with dual modulation and an argon flow was used to ion mill the discs until an electron-transparent specimen was obtained. Before transmission electron microscopy (TEM) experiments, the specimens were cleaned using a Fischione 1020 Plasma Cleaner for 5 min to reduce carbon contamination during data acquisition.

A JEOL 2100F microscope operated at 200 kV was used for acquiring bright-field (BF) and dark-field (DF) STEM images, along with energy-dispersive X-ray spectroscopy (EDS). The microscope is fitted with an Oxford X-max 80SDD EDS detector with a solid angle of 0.23 sr. A double-corrected coldFEG JEOL ARM200F microscope was used for high-resolution (HR)-STEM and EDS experiments. A Centurio SDD EDS detector with a solid angle of 0.98 sr was used for EDS signal detection. The HR-STEM images were obtained at a probe size of 8 \AA and a camera length of 8 cm using JEOL bright-field and dark-field detectors.

3 Results and discussion

3.1 Phase transformations during heating to the solution treatment temperature

Figure 1 a) presents all HE-XRD data collected during the heating of hot rolled steel X5CrNiCuNb16-4 at 0.1 K/s in a 2D contour diagram. At the beginning of the investigation, martensite is the only phase detected, yielding diffraction intensities at 25 keV {110}, 36 keV {200}, 43 keV {211}, 50 keV {220}, and 66 keV {321} for the respective lattice planes. Martensite remains the only detected phase in the material up to approximately 600 $^{\circ}\text{C}$, after which a phase with an FCC crystal structure is observed at 24 keV {111}, 28 keV {200}, 41 keV {220}, 46 keV {311}, and 49 keV {222}. This phase is interpreted to be austenite and its presence is rationalised by the existence of the reverse martensite-to-austenite transformation. Nevertheless, copper precipitates, which are known to form in the martensitic phase during

heating, share very similar lattice spacings and cannot be distinguished from austenite. Consequently, they may contribute to the diffracted intensity of the fcc phase.

The evolution of the fcc austenite (and Cu) phase fraction with respect to the temperature is shown in Figure 1 b). As previously mentioned, at the beginning of the investigation the fraction of austenite is negligible and remains so upon heating up to 600 °C. During continuous heating, the transformation suddenly accelerates at approximately 660 °C, showing a maximum rate at about 710 °C. Subsequently, the transformation slows down, reaching a minimum rate at about 810 °C. Following this, a slight acceleration is observed, with the transformation continuing notably quickly in the temperature range of 850–960 °C, signalling the onset of a second stage of the transformation process. Finally, at about 980 °C, the transformation reaches completion and the crystal structure is 100 % fcc austenite. It is noteworthy that, as discussed later, at this temperature, all Cu is completely re-dissolved into the lattice of the matrix.

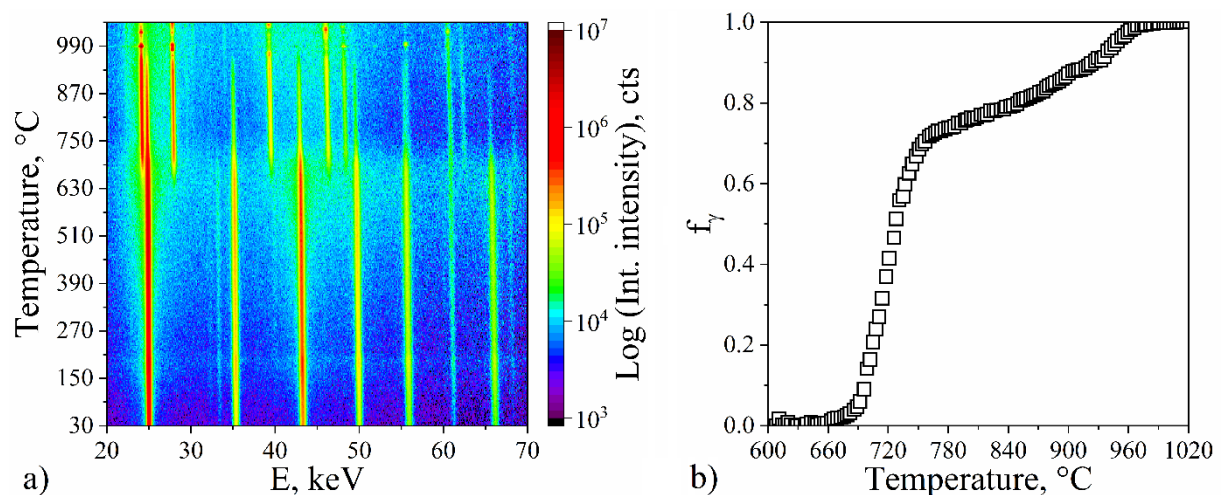


Figure 1: HE-XRD measurements at BESSY II synchrotron facility at the EDDI beamline on hot rolled steel X5CrNiCuNb16-4; a) contour plot at 0.1 K/s; b) development of fraction of austenite during heating at 0.1 K/s.

A two-stage austenitization process was previously reported for the reverse transformation from martensite to austenite in a super-martensitic stainless steel [24], the chemistry of which largely corresponds to that of the steel applied in the present investigation (i.e., 15Cr-5Ni-1Mo compared with 16Cr-4Ni-3Cu). The two-stage austenitization process is characterised by a change in the rate-controlling mechanism during continuous heating, with the diffusion of Ni in martensite controlling the rate of transformation at low temperatures, while Ni diffusion in austenite controls the rate of transformation at high temperatures. In the present case, the redistribution of Cu may also play a role in controlling the kinetics. Cu may be present in the form of fcc precipitates at the beginning of the austenitization process. These precipitates are expected to progressively dissolve during continuous heating. To clarify the evolution of the Cu redistribution in the material, complementary dilatometry and DSC investigations were performed.

A complementary experimental validation by indirect dilatometry involved austenitizing samples at various temperatures between 700 and 1050 °C. The martensite formation during subsequent cooling at a constant rate of 3 K/s is assessed to examine the following postulation: if the above conclusion regarding the two-step austenitization being complete at 950 °C is correct, the different annealing temperatures below 950 °C should cause various fractions of austenite to form with varying composition. These variations would be reflected in the dilatometry curves on subsequent cooling—the varying composition would lead to a variation in the martensite start temperatures (M_s). Moreover, the varying fraction of austenite should cause a varying overall volumetric effect of martensite formation. Indeed, the dilatometer curves shown in Figure 2 can be separated into two groups of curves: (1) for annealing temperatures below 950 °C an increasing M_s is found in combination with a reduced expansion of the samples below M_s . This hints at incomplete austenite transformation in combination with an austenite phase which is lean in solute elements, e.g., Cu. (2) For annealing temperatures higher than 950 °C, no variation of M_s nor volumetric effect is visible, indicating the completion of austenite formation during the annealing step. It has earlier been proven by DSC that the dissolution of Cu-rich phases is also complete at 950 °C [11]. Thus, both structural transformation processes—austenite formation and Cu dissolution—end at the same temperature, which is reasonable because the solubility of Cu in Fe is larger in the fcc austenite phase.

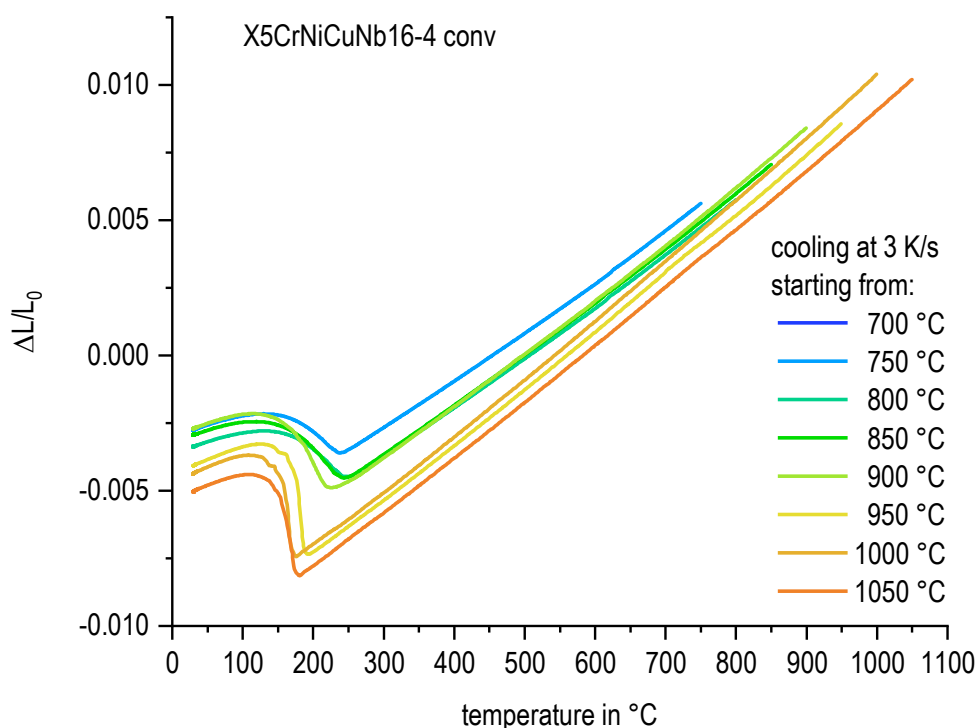


Figure 2: Dilatometer curves for cooling of hot rolled steel X5CrNiCuNb16-4 at a constant rate of 3 K/s after previously approaching different maximum temperatures.

Figure 3 shows the updated CHT diagram based on former DSC and dilatometer experiments [9–11], as well as recent results from HE-XRD and dilatometry. The major update comprises the temperature at which austenite formation is complete, which now equals the temperature at which Cu dissolution is complete.

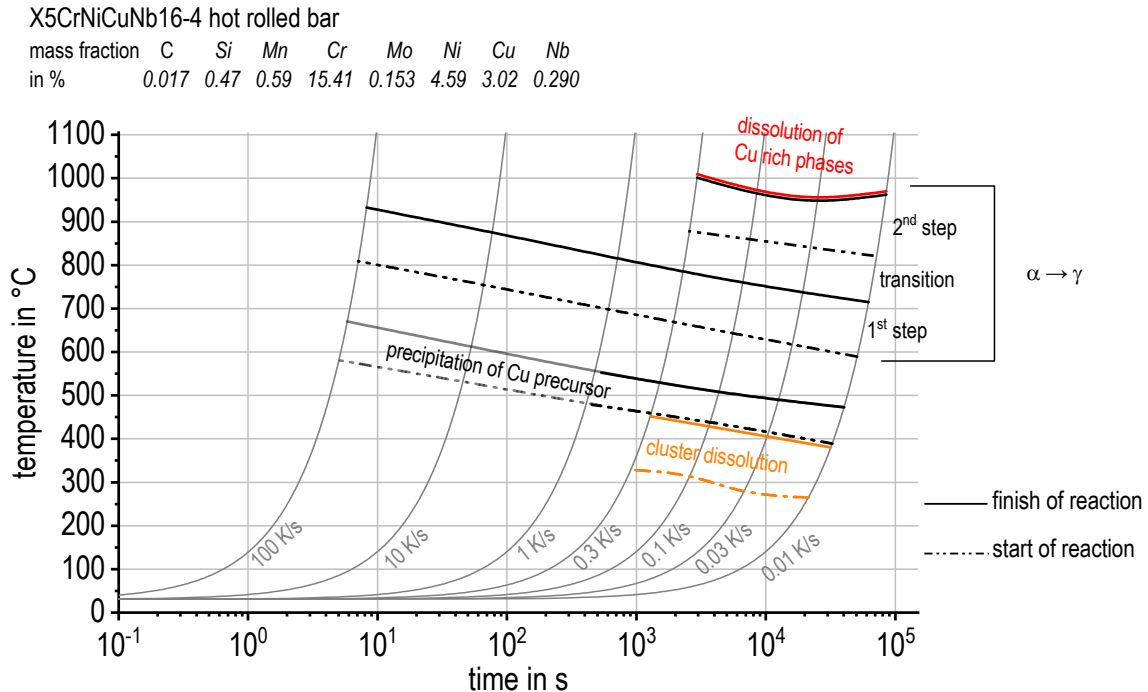


Figure 3: Continuous heating transformation diagram for hot rolled steel X5CrNiCuNb16-4 – initial condition annealed (1038 °C, 1 h) and rapidly quenched by air (dimensions Ø 15 x 3000 mm).

3.2 Quench-induced precipitation of Cu-rich phases during continuous cooling from the solution treatment

All work on continuous cooling is done on the LBM variant of steel X5CrNiCuNb16-4. Due to previous solution annealing (austenitizing) at 1100 °C for 30 min, this material behaves similarly to the hot rolled bar. A comparison of the kinetic precipitation behaviour based on cooling DSC experiments for both batches is published in [9]. Figure 4a) shows DSC cooling curves for the LBM variant with an extended cooling rate range. DSC reveals two subsequent precipitation reaction peaks during continuous cooling (Peak I and Peak II). With increasing cooling rate, these reactions undergo a kinetic shift that is highly similar to that of other metallic alloy systems, showing precipitation hardening like certain Al and Mg alloys [25]. In particular, the first reaction at higher temperatures is increasingly suppressed with increasing cooling rate. Therefore, the remaining concentration of alloying elements at lower temperatures is continuously increased, causing a stronger intensity of the subsequently precipitated phase. This leads to an initial shift of the start temperature of reaction Peak II to higher temperatures. Only during cooling at 0.1 K/s and 0.3 K/s does reaction Peak II occur. Reaction Peak II is now increasingly suppressed for kinetic reasons and consequently shifts to lower temperatures.

Figure 4b) plots the hardness in the as-quenched and artificially aged conditions. Artificial ageing is done at 480 °C for 60 min. From the hardness tests in the aged condition, it is seen that full age hardening potential is achieved only at rates faster than the upper critical cooling rate of about 10 K/s. Additionally in the as-quenched condition, a slight maximum of the hardness at a rate of about 1 K/s is seen, potentially indicating that quench-induced precipitates have precipitated in a favourable ratio of size to number density, resulting in 25 HV higher hardness compared to faster or slower cooling rates. In this order of cooling rates, only reaction Peak II occurs. This indicates that the quench-induced precipitates, which cause a direct hardening contribution, originate from this second quench-induced precipitation reaction.

In former work [11] we have shown that during the first reaction (Peak I), at higher temperatures the precipitation of coarse particles occurs, with dimensions ranging from several μm at 0.0001 K/s to about 100 nm at 0.01 K/s. These particles have been analysed by optical microscopy (OM) and SEM-EDS. In OM they appear Cu-coloured and have a clear enrichment in Cu compared to the matrix [11]. The evidence for the crystal structure of these coarser precipitates is taken indirectly from in situ continuous cooling HE-XRD experiments using the same experimental setup as in [20,26]. During these experiments in the temperature regions of reaction Peaks I and II (as observed in DSC), aside from the reflections of the fcc austenite phase, no extra diffraction reflections were observed. Knowing that fcc austenite and fcc Cu share nearly identical lattice parameters, we conclude that the precipitated phase has the same crystal structure as the matrix and is thus not detected by the HE-XRD measurements. Therefore, we conclude that the coarse Cu-rich precipitates imaged by OM and SEM have a Cu fcc structure. Moreover, compared with other alloy systems [25], it is very likely that the coarse precipitates from reaction Peak I at higher temperatures belong to the equilibrium phase.

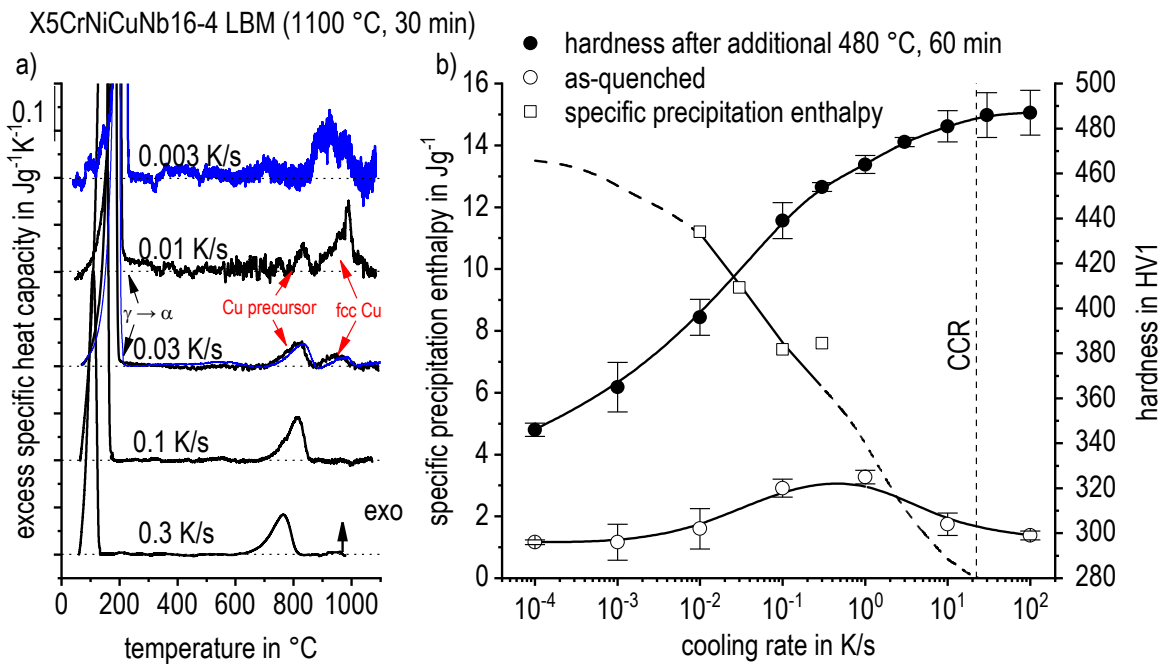


Figure 4: a) DSC cooling curves of LBM steel X5CrNiCuNb16-4 (black curves, 0.01 to 0.3 K/s: Setaram Labsys; blue curves 0.003 and 0.03 K/s: Setaram MultiHTC) and b) specific precipitation enthalpy and hardness in the as-quenched and artificially aged conditions.

Moreover, it is likely that a range of much finer precipitates originating from reaction Peak II is present at the nanoscale. The nanostructure of the X5CrNiCuNb16-4 LBM material after solution annealing (austenitizing at 1100 °C for 30 min) and subsequent cooling at various rates was analysed by ex situ STEM and in situ SAXS.

Figure 5 shows continuous SAXS measurements during cooling at 0.3 K/s. From the DSC results given in Figure 4, it is known that at this cooling rate, only reaction Peak II starting at about 800 °C occurs. SAXS reveals precipitation of particles with dimensions of 3–6 nm starting from about 800 °C, which fits the onset temperature found by DSC. The particle dimensions analysed from SAXS are also in good agreement with the below STEM results of slightly slower cooling rates. Moreover, the quench-induced precipitation of particles with dimensions of a few nm found by SAXS justifies the peak in the as-quenched hardness tests seen in Figure 4 b) for cooling rates of about 0.1–1 K/s. To get an idea of the volume fraction of the related particles, the SAXS data has further been evaluated assuming different chemical compositions of the small particles, as shown in Figure 6. Assuming pure copper, the final volume fraction amounts to about 1.3%.

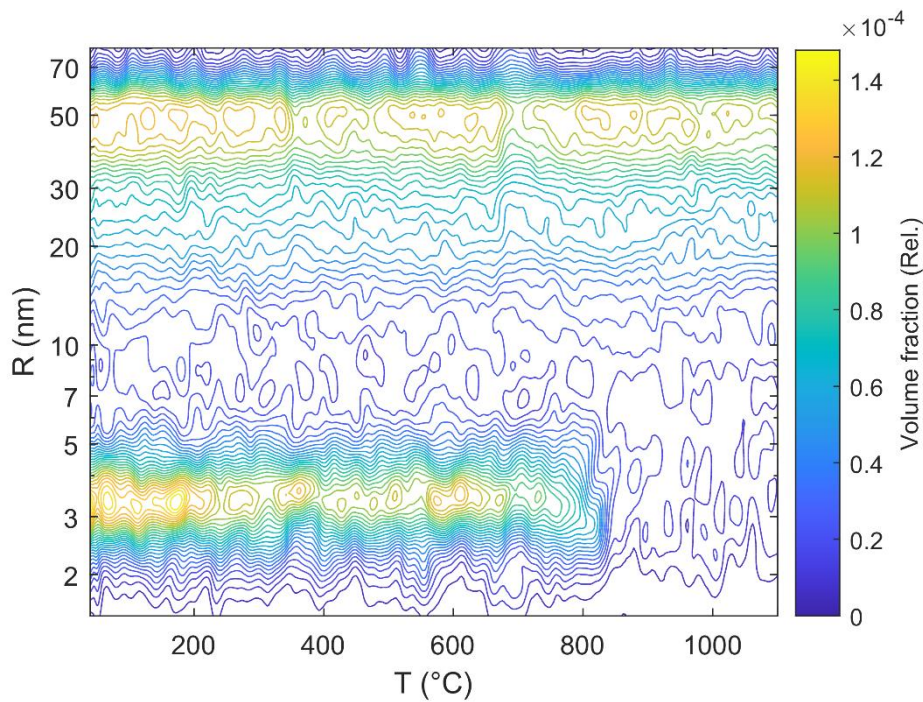


Figure 5: SAXS data during cooling of X5CrNiCuNb16-4 LBM at 0.3 K/s, the colour scale bases on the assumption of the formation of particles from pure Cu.

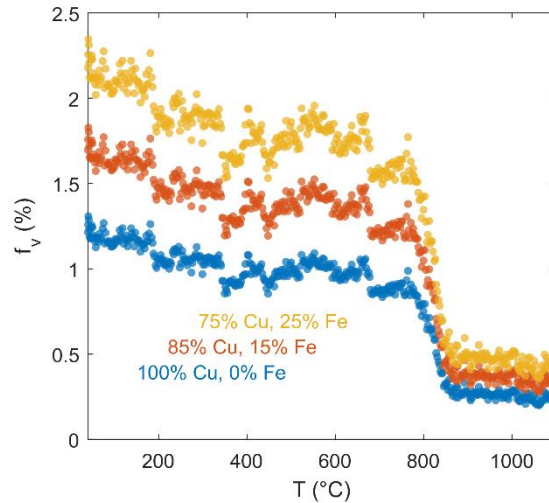


Figure 6: SAXS evaluation on a sample of X5CrNiCuNb16-4 LBM cooled at 0.03 K/s: volume fraction of Cu precursors particles assuming different Cu contents.

Figure 7 shows a high-angle annular dark-field (HAADF)-STEM image of a sample cooled at 0.03 K/s. Several Cu-rich particles are seen. On average, the Cu particles at this cooling rate have a size on the order of several tens of nm. EDS measurements from several similar particles reveal an increased Cu content compared to the measurement from a region without the particles, as shown by the EDS spectrum from the particle and matrix shown in Figure 7 a)

which is plotted in Figure 7 b). The Cu:Fe atomic percentage ratio from EDS measurements varies from 4.41 to 0.47 when the spectrum is collected from a region containing particles. A Cu:Fe atomic percentage ratio of 0.04 was measured when the spectrum was collected from a region that did not contain any visible precipitate particles.

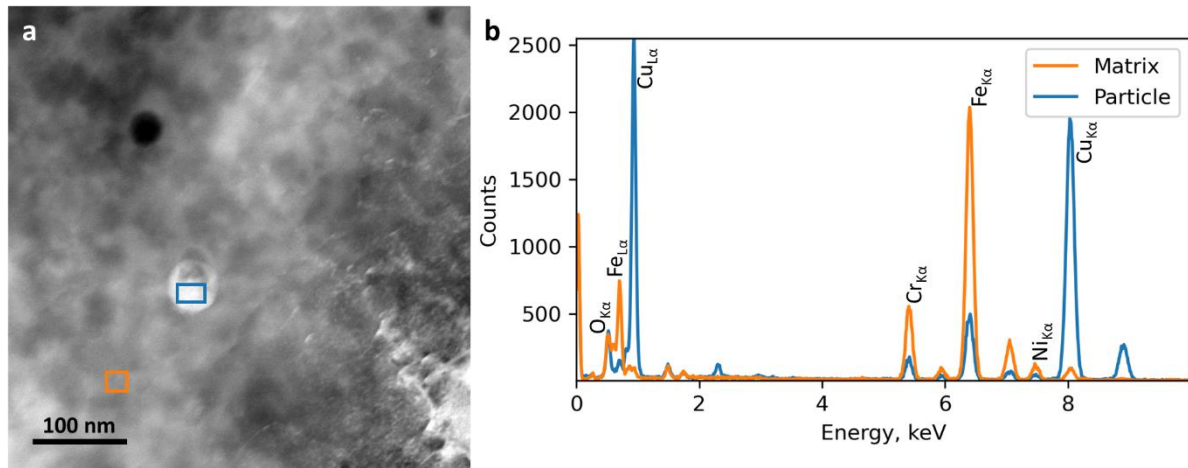


Figure 7: a) STEM image of a Cu particle embedded in steel matrix in a sample cooled at 0.03 K/s. The EDS spectra from the areas marked by the blue and orange boxes are given in b), revealing that the particle contains a high quantity of Cu. A Cu:Fe atomic ratio of 4.41 is found in this spectrum.

Figure 8 shows bright-field STEM images and Cu EDS maps comparing two cooling conditions of 0.1 and 1 K/s. After cooling at 0.1 K/s, a relatively high number density of distinct Cu particles with an average diameter of 16 nm was observed. After cooling at 1 K/s, the Cu particles were even smaller, with diameters between 3 and 6 nm.

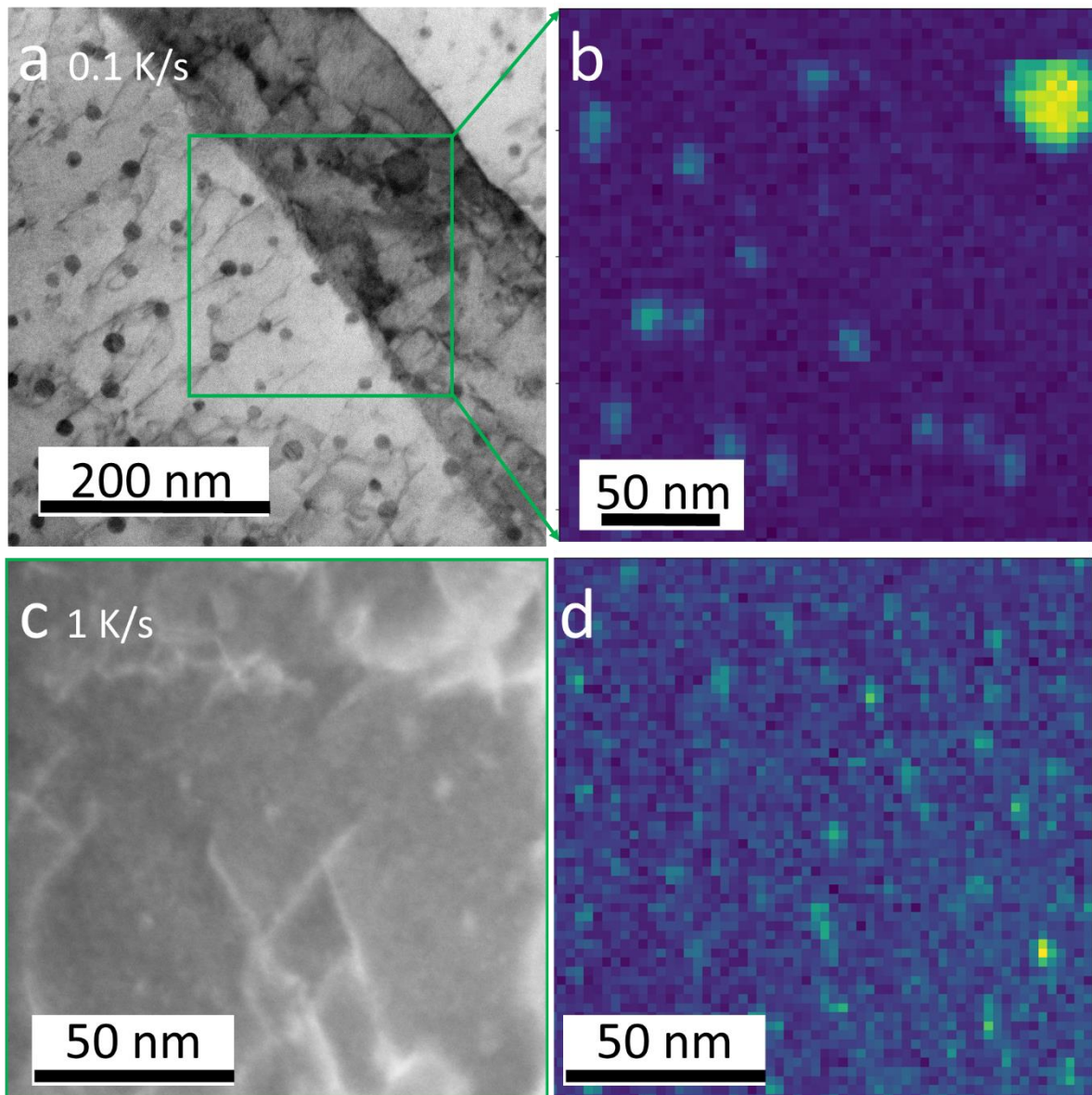


Figure 8: a) and c) BF STEM images of Cu particles embedded in the steel matrix, while b) and d) show the corresponding EDS maps using the Cu signal from the area marked green. In a) and b) a sample cooled at 0.1 K/s is analysed, while c) and d) show a sample cooled at 1 K/s.

Figure 9 shows HAADF-STEM images from four cooling conditions: 0.03 K/s, 0.1 K/s, 1 K/s, and 10 K/s. In general, it is seen that the dimensions of the Cu-enriched precipitates decrease as the cooling rate increases. It appears that no quench-induced precipitates are found after cooling at 10 K/s. This is in good correlation with the results given in Figure 4. From the hardness after ageing, the upper critical cooling rate is about 10 K/s. Therefore, after cooling, it is reasonable not to find any quench-induced precipitates via STEM. DSC shows decreasing precipitation enthalpies with increasing cooling rates, which relates to the volume fraction of precipitates formed. The larger volume fraction after cooling at slower rates correlates to a reduced number density of coarser precipitates. At higher rates, an increased number of smaller particles is formed.

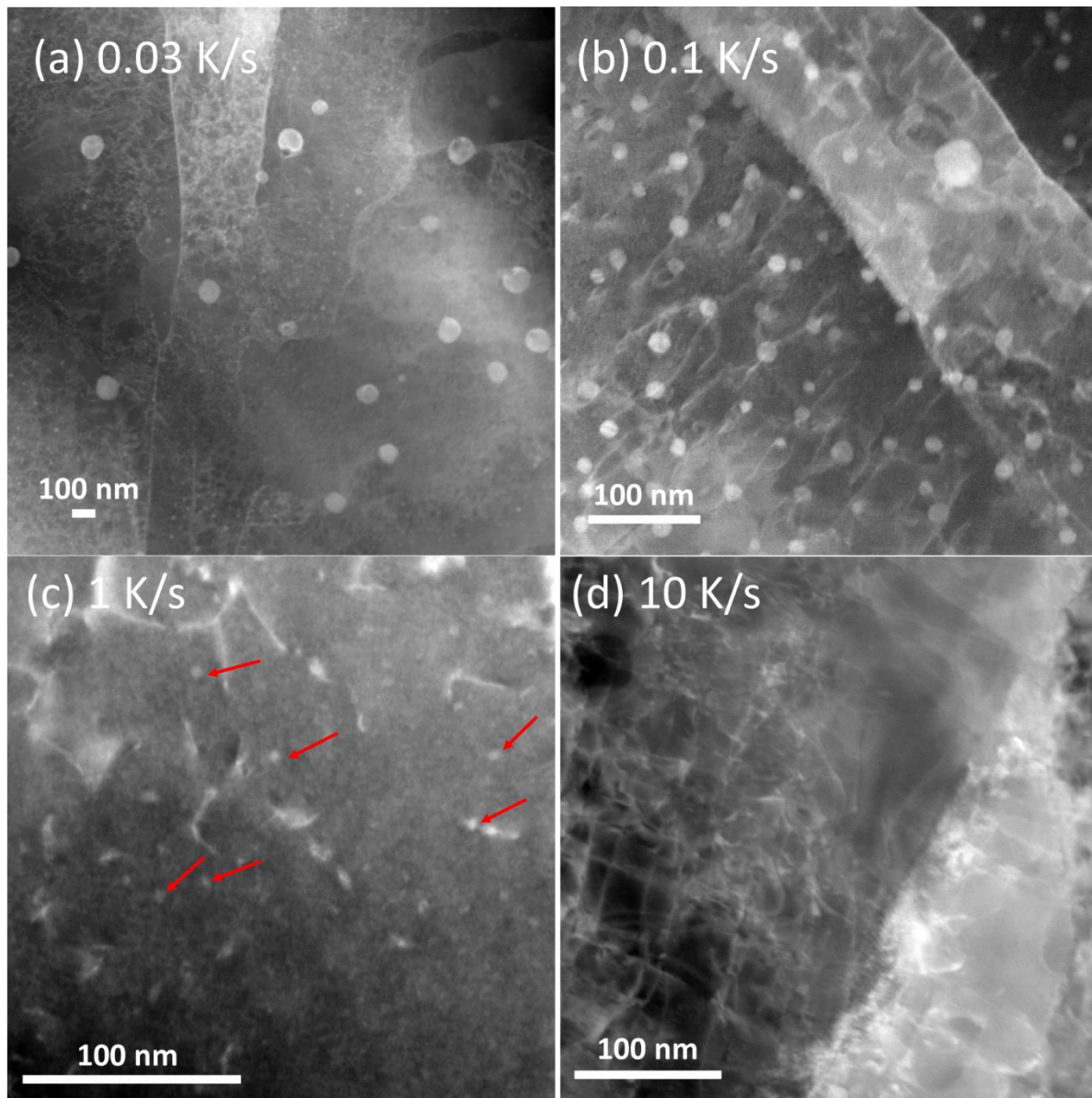


Figure 9: HAADF-STEM overview for a broad range of cooling rates from 1100 °C to room temperature: a), b), c) and d) are representative HAADF-STEM images from the samples quenched at 0.03, 0.1, 1, and 10 K/s, respectively. In d), the sample was cooled at 10 K/s and Cu particles could not be detected, instead the contrast is due to a high dislocation density. In c), fine Cu particles are seen as bright contrast (marked by the arrows), with EDS confirming Cu enrichment. At 0.1 K/s, b) shows Cu-rich particles with an average diameter of 16 nm. At 0.03 K/s, a) shows larger Cu particles along with smaller Cu particles, with the average size measured to be 70 nm.

Atomic resolution STEM images of some smaller Cu-rich particles of a sample cooled at 0.1 K/s were investigated from three different zone axes of the steel matrix, namely $\langle 001 \rangle$, $\langle 011 \rangle$, and $\langle 111 \rangle$. During cooling at 0.1 K/s, reaction Peak I is fully suppressed, while reaction Peak II reaches its intensity maximum, as displayed in Figure 4. Therefore, we conclude that the particles shown in Figure 10 originate from reaction Peak II. For all three zone axes, the Cu particles were perfectly resolved with the same lattice spacings and orientation as the matrix, as shown in Figure 10. Fast Fourier transformations (FFTs) were performed on the square regions of interest, indicated by red boxes, from both the matrix and the particles across

all three zones. It was found that both the particle and the matrix were at identical orientations and had the same lattice spacings in all three cases. This proves that the Cu particles have the same crystal structure as the martensitic matrix, which is bcc in this case. In other words, the Cu-rich particles up to dimensions of about 10 nm are nearly fully coherent with the bcc matrix from the $\langle 001 \rangle$, $\langle 011 \rangle$, and $\langle 111 \rangle$ Fe-bcc zone axes. Remarkably, these particles have formed at around 850–700 °C in the fcc austenite matrix (Figure 4), which then transformed to bcc martensite below 200 °C. Thus, the precipitation happened in an fcc austenitic matrix phase which later transformed to bcc, in which the particles are now found to be coherent. From the literature on austenitic Cu precipitation-hardening steels, it is known that precipitation happens as coherent fcc Cu almost independently of the ageing state [27–30].

We assume that the smaller Cu particles originally precipitate as fcc Cu and then change simultaneously with the matrix transformation to bcc Cu, thereby remaining fully coherent with the matrix. Another batch of steel X5CrNiCuNb16-4 with comparable chemical composition was solution annealed at 1.050 °C for 0.5 h and subsequently isothermally aged in an austenitic condition at 700 °C for various durations before quenching [31]. It was found that Cu clusters, as well as fully coherent fcc Cu precipitates, develop in the fcc austenite matrix. However, during quenching, the fcc austenite lattice transforms martensitically into bcc. For a precipitate size of up to 4–5 nm, Cu particles remain coherent and transform to bcc together with the matrix [31]. In earlier works, this scenario was also found to occur for a precipitate size up to 4–5 nm [32,33]. However, for Fe-7Al-2C particles, this simultaneous particle transformation is observed for particles exceeding 5 nm [34]. In the present work, it appears that even Cu particles up to about 10 nm in diameter can transform simultaneously with the martensitic transformation of the matrix. This aspect should be further investigated.

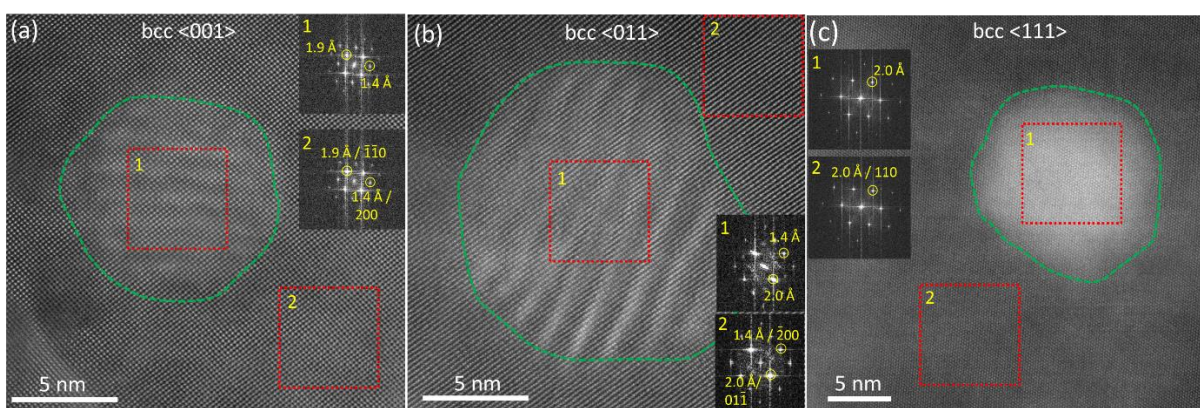


Figure 10: High-resolution HAADF-STEM images of Cu particles embedded in the steel matrix of the 0.1 K/s cooled sample acquired at the $\langle 001 \rangle$, $\langle 011 \rangle$, and $\langle 111 \rangle$ zone axes of the bcc steel matrix are presented in a), b), and c), respectively. The Cu particles are marked by the dotted green loops. FFTs of the regions marked by the red boxes are presented in the insets. In each case, the FFT from particle (1) and matrix (2) are inspected. It was found that the lattice plane spacings and the orientation were exactly the same from both (1) and (2) in all three zone axes. This proves that the embedded Cu particles had the same bcc structure as the steel matrix. Contrast similar to Moiré fringes can be seen in the particles in a) and b), which could be caused by dislocations or small differences in lattice plane spacings.

All the experimental results on precipitation and transformation during continuous cooling in a wide range of cooling rates are used to plot the updated CCT diagram, which is displayed in Figure 11.

X5CrNiCuNb16-4 LBM; austenitisation 1100 °C, 30 min

| mass fraction | C | Si | Mn | Cr | Mo | Ni | Cu | Nb |
|---------------|-------|------|------|-------|-------|------|------|-------|
| in % | 0.013 | 0.34 | 0.22 | 16.65 | 0.014 | 4.32 | 4.15 | 0.296 |

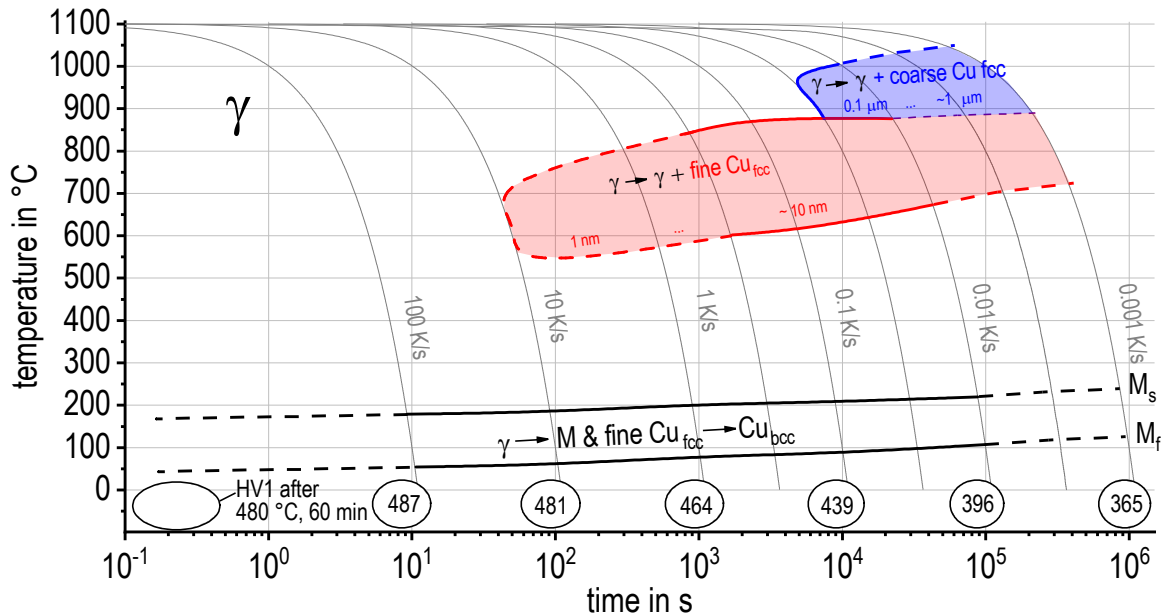


Figure 11: Continuous cooling transformation diagram for LBM steel X5CrNiCuNb16-4.

4 Conclusions

Based on in situ DSC, dilatometry, HE-XRD, and SAXS during heating and cooling, as well as ex situ hardness testing, OM, SEM, and STEM of the martensitic, precipitation-hardening steel X5CrNiCuNb16-4, we draw the following conclusions on the relevant phase transformations:

- During heating, the transformation of martensite to austenite and the dissolution of Cu-rich secondary phases are completed at the same temperature. The continuous heating transformation (CHT) diagram has been updated accordingly.
- During cooling, quench-induced precipitation occurs in two distinct reactions, both of which likely precipitate the same phase, i.e., fcc Cu.
 - o Quench-induced precipitation of coarse fcc Cu particles (dimensions at 0.0001 K/s up to several μm and at 0.03 K/s up to 100 nm) happens in a temperature range of about 1030–900 °C. This reaction is fully suppressed at cooling rates faster than about 0.1 K/s.

- Precipitation of fine fcc Cu particles (dimensions at 0.1 K/s up to about 15 nm and at 1 K/s up to about 5 nm) in a temperature range of about 900–600 °C. This reaction is fully suppressed at cooling rates faster than about 10 K/s.
 - Fine fcc Cu particles transfer to bcc Cu simultaneously with the martensite transformation at temperatures below M_s . For particles with an average size between 5 and 10 nm, a bcc structure which is fully coherent with the Fe martensite matrix was observed by STEM at three different zone axes.
 - The exact composition of the precipitate particles remains unclear; however, a clear enrichment in Cu is proven by SEM-/STEM-EDS.
- The continuous cooling transformation (CCT) diagram has been completed through the addition of quench-induced precipitate phases and particle dimensions.
 - Steel X5CrNiCuNb16-4 is found to be quench sensitive. Its full age hardening potential can only be exploited if cooling is done faster than the upper critical cooling rate, which is about 10 K/s.
 - In general, the kinetic development of quench-induced precipitation, including the kinetic shift of single reactions, is highly similar to other precipitation-hardening alloy systems like age-hardening Al alloys. Quench-induced precipitation is increasingly suppressed with increasing cooling rate and the particle size decreases with increasing cooling rate.

Acknowledgements

The authors acknowledge the granted measurement time at the high energy materials science beamline P07 at PETRA III, Deutsches Elektronen-Synchrotron, Hamburg, Germany (Proposal I-20170023) and the helpful support of the DESY staff.

The authors would like to thank Hannes Fröck (Chair of Materials Science, University of Rostock) for performing continuous cooling DSC experiments using the Setaram MultiHTC. The German Federal Ministry of Economic Affairs and Climate Action, BMWK (formerly BMWi) is acknowledged for funding of the Setaram MultiHTC DSC device within the Project MarKomp (BMW i 03SX507C).

This project has received funding from the European Union's Horizon 2020 research and innovation program under grant agreement No 823717 – ESTEEM3. The related TEM work was done using the NORTEM instruments at NTNU in Trondheim (Norwegian Research Council project number 197405).

Data availability

The raw/processed data required to reproduce these findings cannot be shared at this time as the data also forms part of an ongoing study.

5 References

- [1] F.E. Mariani, G.S. Takeya, L.C. Casteletti, A.L. Neto, G.E. Totten, Heat treatment of precipitation-hardening stainless steels alloyed with niobium, *Mater Perform Charact* 5 (2016) 38–46. <https://doi.org/10.1520/MPC20150039>.
- [2] M. Hofinger, C. Turk, M. Ognianov, H. Leitner, R. Schnitzer, Precipitation reactions in a Cu-Ni-Al medium carbon alloyed dual hardening steel, *Mater Charact* 160 (2020). 110126. <https://doi.org/10.1016/j.matchar.2020.110126>.
- [3] K.J. Irvine, D.T. Llewellyn, F.B. Pickering, Controlled-transformation stainless steels, *J Iron Steel Inst* 192 (1959) 218–238.
- [4] D. Huang, J. Yan, X. Zuo, Co-precipitation kinetics, microstructural evolution and interfacial segregation in multicomponent nano-precipitated steels, *Mater Charact* 155 (2019). 109786. <https://doi.org/10.1016/j.matchar.2019.06.028>.
- [5] G. Han, Z.J. Xie, Z.Y. Li, B. Lei, C.J. Shang, R. Misra, Evolution of crystal structure of Cu precipitates in a low carbon steel, *Mater Des* 135 (2017) 92–101. <https://doi.org/10.1016/j.matdes.2017.08.054>.
- [6] P.J. Othen, M.L. Jenkins, G.D.W. Smith, W.J. Phythian, Transmission electron microscope investigations of the structure of copper precipitates in thermally-aged Fe—Cu and Fe—Cu—Ni, *Phil Mag Let* 64 (1991) 383–391. <https://doi.org/10.1080/09500839108215121>.
- [7] P.J. Othen, M.L. Jenkins, G.D.W. Smith, High-resolution electron microscopy studies of the structure of Cu precipitates in α -Fe, *Phil Mag* 70 (1994) 1–24. <https://doi.org/10.1080/01418619408242533>.
- [8] L. Couturier, F. De Geuser, M. Descoins, A. Deschamps, Evolution of the microstructure of a 15-5PH martensitic stainless steel during precipitation hardening heat treatment, *Mater Des* 107 (2016) 416–425. <https://doi.org/10.1016/j.matdes.2016.06.068>.
- [9] C. Rowolt, B. Milkereit, M. Gebauer, C. Seidel, B. Müller, O. Kessler, In-Situ Phase Transition Analysis of Conventional and Laser Beam Melted AlSi10Mg and X5CrNiCuNb16-4 Alloys, *HTM - Journal of Heat Treatment and Materials* 73 (2018) 317–334. <https://doi.org/10.3139/105.110366>.
- [10] C. Rowolt, B. Milkereit, P. Andreatza, O. Kessler, Quantitative High Temperature Calorimetry on Precipitation in Steel and Nickel Alloys, *Thermochim Acta* 677 (2019) 169–179. <https://doi.org/10.1016/j.tca.2019.01.026>.
- [11] C. Rowolt, B. Milkereit, A. Springer, C. Kreyenschulte, O. Kessler, Dissolution and precipitation of copper-rich phases during heating and cooling of precipitation hardening steel X5CrNiCuNb16-4 (17-4 PH), *Journal of Materials Science* 55 (2020) 13244–13257. <https://doi.org/10.1007/s10853-020-04880-4>.
- [12] C. Rowolt, *Untersuchungen zur Wärmebehandlung additiv gefertigter, metallischer Bauteile auf Basis von in-situ Analysen der Phasenumwandlungen*, Universität Rostock, 2020.
- [13] M. Reich, B. Milkereit, M. Bader, H.G. Oehmigen, O. Kessler, Calorimetric and Dilatometric Study of Tempering Behavior in the Heat Affected Zone of T24 Welding Seams, *HTM - Journal of Heat Treatment and Materials* 68 (2013) 274–282. <https://doi.org/10.3139/105.110202>.
- [14] Verein Deutscher Eisenhüttenleute, *Richtlinien für Vorbereitung, Durchführung und Auswertung dilatometrischer Umwandlungsuntersuchungen an Eisenlegierungen*, Stahleisen m.b.H., Düsseldorf, 1993.
- [15] E. Calvet, H. Prat, H. Skinner (Eds.), *Recent progress in microcalorimetry*, Pergamon Press, Oxford, London, New York, Paris, 1963.

- [16] C. Genzel, I.A. Denks, M. Klaus, The Materials Science Beamline EDDI for Energy-Dispersive Analysis of Subsurface Residual Stress Gradients, *Mater Sci Forum* 524-525 (2006) 193–198. <https://doi.org/10.4028/www.scientific.net/MSF.524-525.193>.
- [17] B.C. Giessen, G.E. Ordon, X-ray diffraction: new high-speed technique based on x-ray spectrography, *Science (New York, N.Y.)* 159 (1968) 973–975. <https://doi.org/10.1126/science.159.3818.973-a>.
- [18] E.S.U. Laine, A high-speed determination of the volume fraction of ferrite in austenitic stainless steel by EDXRD, *Journal of Physics F: Metal Physics* 8 (1978) 1343–1348. <https://doi.org/10.1088/0305-4608/8/7/007>.
- [19] F. Nießen, M. Villa, D. Apel, O. Keßler, M. Reich, J. Hald, M.A. Somers, In Situ Techniques for the Investigation of the Kinetics of Austenitization of Supermartensitic Stainless Steel, *Mater Sci Forum* 879 (2016) 1381–1386. <https://doi.org/10.4028/www.scientific.net/MSF.879.1381>.
- [20] C. Rowolt, H. Fröck, B. Milkereit, M. Reich, W. Kowalski, A. Stark, O. Kessler, In-situ analysis of continuous cooling precipitation in Al alloys by wide-angle X-ray scattering, *Science and technology of advanced materials* 21 (2020) 205–218. <https://doi.org/10.1080/14686996.2020.1739554>.
- [21] N. Schell, A. King, F. Beckmann, T. Fischer, M. Müller, A. Schreyer, The High Energy Materials Science Beamline (HEMS) at PETRA III, *Mater Sci Forum* 772 (2013) 57–61. <https://doi.org/10.4028/www.scientific.net/MSF.772.57>.
- [22] F. Zhang, J. Ilavsky, G.G. Long, J.P.G. Quintana, A.J. Allen, P.R. Jemian, Glassy Carbon as an Absolute Intensity Calibration Standard for Small-Angle Scattering, *Metall Mater Trans A* 41 (2010) 1151–1158. <https://doi.org/10.1007/s11661-009-9950-x>.
- [23] I. Bressler, B.R. Pauw, A.F. Thunemann, McSAS: software for the retrieval of model parameter distributions from scattering patterns, *J Appl Crystallogr* 48 (2015) 962–969. <https://doi.org/10.1107/S1600576715007347>.
- [24] F. Niessen, M. Villa, J. Hald, M.A. Somers, Kinetics analysis of two-stage austenitization in supermartensitic stainless steel, *Mater Des* 116 (2017) 8–15. <https://doi.org/10.1016/j.matdes.2016.11.076>.
- [25] B. Milkereit, M.J. Starink, P.A. Rometsch, C. Schick, O. Kessler, Review of the Quench Sensitivity of Aluminium Alloys: Analysis of the Kinetics and Nature of Quench-Induced Precipitation, *Materials* 12 (2019) 1–92. <https://doi.org/10.3390/ma12244083>.
- [26] H. Fröck, C. Rowolt, B. Milkereit, M. Reich, W. Kowalski, A. Stark, O. Kessler, In situ high-energy X-ray diffraction of precipitation and dissolution reactions during heating of Al alloys, *J Mater Sci* (2021) 19697–19708. <https://doi.org/10.1007/s10853-021-06548-z>.
- [27] T. Xi, M. Babar Shahzad, D. Xu, J. Zhao, C. Yang, M. Qi, K. Yang, Copper precipitation behavior and mechanical properties of Cu-bearing 316L austenitic stainless steel: A comprehensive cross-correlation study, *Mater Sci Eng A* 675 (2016) 243–252. <https://doi.org/10.1016/j.msea.2016.08.058>.
- [28] J.W. Bai, P.P. Liu, Y.M. Zhu, X.M. Li, C.Y. Chi, H.Y. Yu, X.S. Xie, Q. Zhan, Coherent precipitation of copper in Super304H austenite steel, *Mater Sci Eng A* 584 (2013) 57–62. <https://doi.org/10.1016/j.msea.2013.06.082>.
- [29] D. Isheim, S. Vaynman, M.E. Fine, D.N. Seidman, Copper-precipitation hardening in a non-ferromagnetic face-centered cubic austenitic steel, *Scripta Mater* 59 (2008) 1235–1238. <https://doi.org/10.1016/j.scriptamat.2008.07.045>.
- [30] L. Ren, J. Zhu, L. Nan, K. Yang, Differential scanning calorimetry analysis on Cu precipitation in a high Cu austenitic stainless steel, *Mater Des* 32 (2011) 3980–3985. <https://doi.org/10.1016/j.matdes.2011.03.068>.
- [31] M. Villa, F.B. Grummen, F. Niessen, T. Dahmen, L. Cao, M. Reich, O. Kessler, X. Huang, M.A. Somers, Aging 17-4 PH martensitic stainless steel prior to hardening:

- effects on martensitic transformation, microstructure and properties, *Materialia* (2023) 101882. <https://doi.org/10.1016/j.mtla.2023.101882>.
- [32] E. Hornbogen, W. Meyer, Martensitische Umwandlung von Mischkristallen mit kohärenten Teilchen, *Acta Metall* 15 (1967) 584–586. [https://doi.org/10.1016/0001-6160\(67\)90099-5](https://doi.org/10.1016/0001-6160(67)90099-5).
- [33] T. Maki, C.M. Wayman, Effect of coherent precipitates in austenite on the martensite substructure in an Fe-Ni-Ti-C alloy, *Acta Metall* 25 (1977) 695–710. [https://doi.org/10.1016/0001-6160\(77\)90012-8](https://doi.org/10.1016/0001-6160(77)90012-8).
- [34] R. Oshima, C. Wayman, Fine structure in quenched Fe-Al-C steels, *Metallurgical Transactions* 3 (1972) 2163–2169. <https://doi.org/10.1007/BF02643228>.